RSC Advances

PAPER

View Article Online
View Journal | View Issue

Cite this: *RSC Adv.*, 2025, **15**, 46425

Water-soluble binuclear aquo Cu(II) complex with an amide ligand as an electrocatalyst for the OER, HER and CO_2RR

Md. Adnan Khan,[a] Sonal Shruti,[a] Swaraj Sengupta,[b] Sahanwaj Khan,[a] Prabhakar Bhardwaj,[c] Pankaj Kumar[c] and Subhendu Naskar *[a]

Received 13th October 2025
Accepted 4th November 2025

DOI: 10.1039/d5ra07824e

rsc.li/rsc-advances

A dinuclear copper complex (**1**) with the formula Cu_2L_2 (where L = [3-((pyridin-2-ylmethyl)carbamoyl) isonicotinic acid]) was synthesized and characterized by single-crystal XRD and mass spectrometry. The complex showed a high order of electrocatalytic hydrogen evolution reaction (HER) and carbon dioxide reduction reaction (CO_2RR) activity in acidic media, along with a moderate oxygen evolution reaction (OER) activity in the pH range of 7 to 13.5. The efficiency of **1** for the HER was calculated as follows: TOF = 1679 s^{-1}, TON = 586 and F.E. = 83% in 56 equivalents of perchloric acid. For the CO_2RR, a TOF value of 4 h^{-1}, a TON of 18 and an F.E. of 92% were observed, with a percentage selectivity of ~99.99% for CO_2 to $(COOH)_2$. The best water oxidation activity was accomplished at pH 13.5 with the following electroanalytical efficacy parameters: TOF = 9 s^{-1} (peak current method), TOF_{FOWA} = 31 s^{-1}, TON = 66 and F.E. = 84%. The high stability of the molecular catalyst was analyzed through CV, FESEM, EDX and DLS.

Introduction

Sustainable generation of carbon-neutral fuels is one of the major milestones mankind has been trying to achieve for decades. The conversion of solar energy to fuels with high calorific values, such as molecular hydrogen and oxygen, can be the solution to major issues like the energy crisis and global warming. The increased CO_2 concentration in the atmosphere, the major cause of global warming, can be tackled by following the natural biochemical outline of photosynthesis *i.e.* converting CO_2 into complex carbohydrates. The abundance of salty water on our planet that is unfit for drinking without treatment has inspired humans to use it for energy generation. Splitting of water through electrolysis generates hydrogen and oxygen through proton reduction and water oxidation, respectively. In this process, the half-reaction of water oxidation is considered the bottleneck since it involves $4e^-$ transfer with several bond rearrangements through proton-coupled electron transfer (PCET). Thus, it is important to develop and employ a catalyst that can mimic PSII with high stability, efficiency and low overpotential. Several previous reports have revealed that Pt,[1,2] Ir,[3] Ru[4] and Rh[5] can achieve higher efficacy in artificial photosynthesis, but their scarce availability, difficulties in mining and high cost have compelled us to find alternatives. Thus, imitating photosynthesis by employing the natural blueprint of photosynthesis using earth-abundant metal-based molecular catalysts is highly desirable. Most of the molecular catalysts reported so far work as homogeneous catalysts upon dissolution in organic solvents.[6–8] This adds both economic and environmental expenses to the process. However, developing water-soluble, first-row transition metal-based molecular catalysts that can oxidize water to molecular oxygen, reduce protons to hydrogen and reduce carbon dioxide to high end products like CH_4, C_2H_4, CH_3CH_2OH, $(COOH)_2$, CH_3COOH and C3 alcohols with greater stability and efficiency is the real quest.[9–12] Therefore, utilizing the abundant and universal solvent, *i.e.* water, for electrochemical catalysis is a favorable solution to such an issue. The unconstrained conversion of CO_2 to a variety of products and low selectivity are major challenges. Therefore, extensive research and investigation of the mechanistic cycle are required for electrochemical CO_2RR as well as HER and OER. The high availability of copper and its great stability make it one of the best candidates for generating hydrogen, oxygen and carbon reduced products.[13–18]

Single-crystal X-ray diffraction analysis

The single crystals of ligand **L1** (CCDC 2388874) and metal complex **1** (CCDC 2388873) were obtained in methanol and DMSO, respectively. The crystallographic data and refinement parameters are presented in Tables S1.1–1.3 and S2.1–2.3 for **L1** and Cu–complex **1**, which demonstrate the selective bond angles and bond lengths, respectively. A triclinic crystal system

[a]*Department of Chemistry, Birla Institute of Technology-Mesra, Ranchi, India. E-mail: subhendu@bitmesra.ac.in*

[b]*Department of Chemical Engineering, Birla Institute of Technology-Mesra, Ranchi, India*

[c]*Department of Chemistry, Indian Institute of Science Education and Research, Tirupati, India*

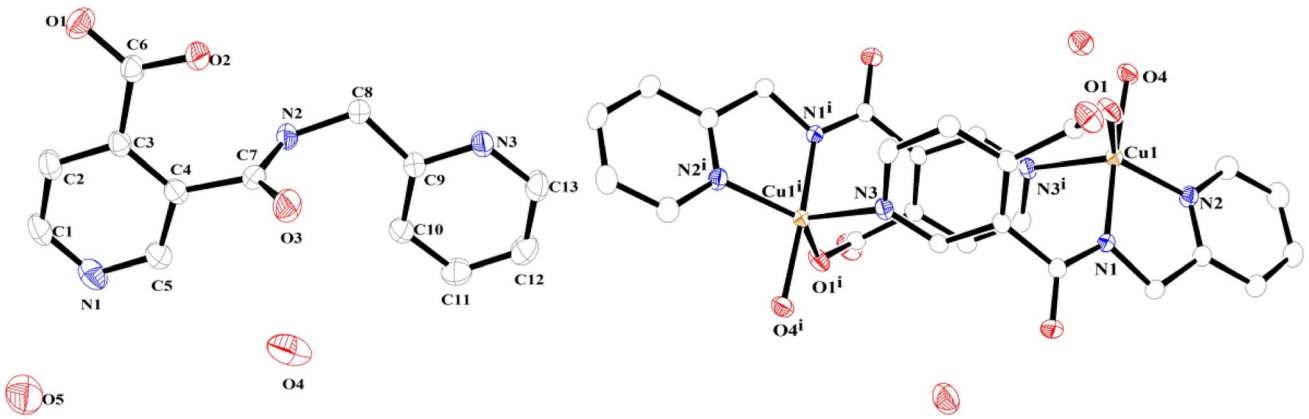

Fig. 1 ORTEP diagram of the ligand **L1** and dinuclear Cu-complex: **1**.

with the $P\bar{1}$ space group was observed for **L1**, whereas the metal complex showed a monoclinic crystal system with the $P2_1/n$ space group. The perspective ORTEP diagrams of both the ligand and metal complex are presented in Fig. 1. A Rigaku Oxford Diffraction X-Calibur CCD system, controlled using CrysalisPro, was used for crystallographic data collection at 298 K. The measurements were made on an Enraf Nonius Kappa CCD diffractometer with Mo-Kα (0.71073 Å). The crystal structure was solved with the Shelxs implemented in the Olex2 software package using Charge Flipping and refined with the SHELXL using Least Squares minimization.[19]

Result and discussion

Synthesis and characterization

This work describes a highly efficient water-soluble copper amide complex, namely the dinuclear aquo copper complex (**1**), which can act as a redox catalyst for water oxidation, and proton and carbon dioxide reduction. The electrocatalytic parameters for proton reduction, carbon dioxide reduction and water oxidation activity are summarized in Table S3 and Fig. S23. The ligand was obtained by the amidation of pyridine 3,4-dicarboxylic acid using 2-amino methyl pyridine. When the ligand was reacted with $Cu(ClO_4)_2$, a binuclear copper complex was formed (SI Scheme 1). Mass spectral analysis of the ligand **L1** and **1** ($Cu_2L_2 \cdot 2H_2O$) revealed their base peaks at $m/z = 258.27$ and $m/z = 673.39$, respectively, which match the expected values (Fig. S1 and S2). The NMR spectrum (Fig. S3) of the ligand and the single-crystal XRD pattern of the ligand with the metal complex are displayed in Fig. 1.

HER study

The electrocatalytic reduction of protons by complex **1** in water was examined by cyclic voltammetry and bulk electrolysis. In the cathodic scan of CV of **1** in an aqueous solution, two quasi-reversible peaks at −0.1 V and −0.75 V *vs.* Ag/AgCl (aqueous) were observed, in agreement with previous reports.[20,21,33] These can be assigned to the $Cu^{II}Cu^{II}/Cu^{II}Cu^{I}$ and $Cu^{II}Cu^{II}/Cu^{I}Cu^{I}$ redox processes, respectively (Fig. 2(A)). The addition of perchloric acid as the source of proton to the catalyst solution produced interesting results, with a continuous increase in the current intensity with incremental addition up to 56 equivalents

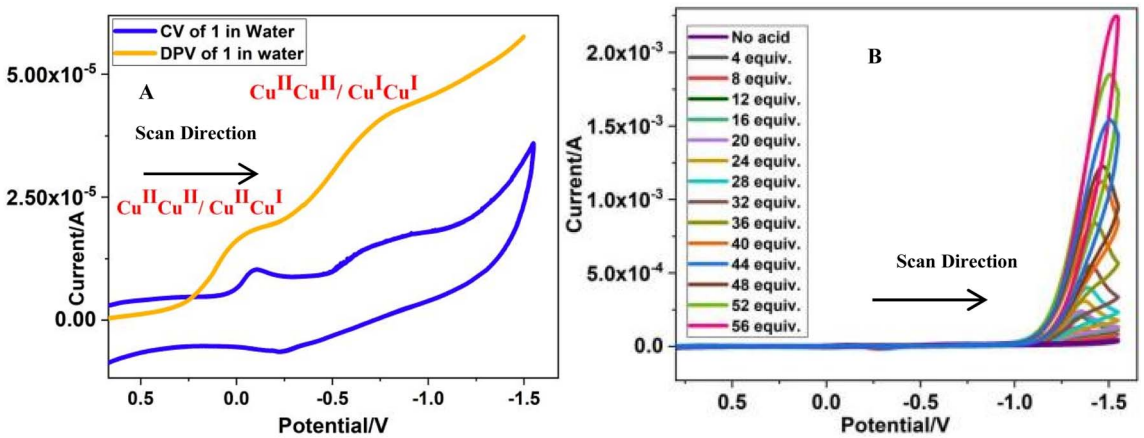

Fig. 2 (A) CV curve and DPV of the cathodic segment of **1** in water; $c = 0.5$ mM, scan rate = 100 mV s^{-1}, internal reference: Ag/AgCl (aqueous), and working electrode: glassy carbon. (B) CV curves of 0.5 mM complex **1** in water with the addition of 0–56 equivalents of perchloric acid.

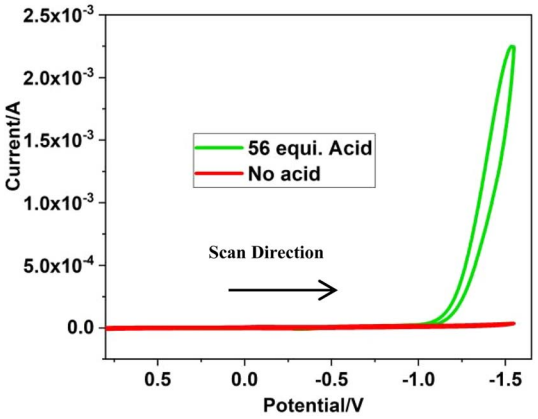

Fig. 3 Comparison of the CV curves of complex **1** in water without acid and with 56 equivalents of acid.

(Fig. 2(B) and 3). Thus, an i_c/i_p value of 91.80 was obtained for **1** at the maximum acid concentration, where i_c is the catalytic peak current with 56 equivalents of perchloric acid, and i_p is the peak current without acid. This resulted in a high TOF of 1679 s^{-1}, as calculated using eqn (A) (where $n = 2$ *i.e.* the number of electrons involved in the catalytic cycle, $R = 8.314$ J K^{-1} mol^{-1}, $T = 298$ K, $\nu = 100$ mV s^{-1}). This implies that the **1** is a highly active catalyst for HER.

In the CV results, it was observed that the peak current of the $Cu^{II}Cu^{II}/Cu^{I}Cu^{I}$ couple continuously improved as the concentration of the acid in the homogeneous catalytic solution increased. To quantify the H_2 generated during catalysis, CPE (controlled potential electrolysis) was carried out for 2 hours at −1.6 V using N_2 to neutralize the atmospheric gases in the working electrode cell. 56 equivalents of perchloric acid are used as the source of protons during CPE. After the completion of CPE, the solution was subjected to mass spectroscopic analysis, and the gas from the headspace was evaluated by gas chromatography. GC detected H_2 with high concentration during the analysis (Fig. S7). The faradaic efficiency was calculated[22,23] as ~83% using the total charge accumulated during 2 hours of CPE and the change in the volume of the catalytic solution in the cell holding the working electrode. The TON of **1** after 2 hours of CPE was calculated using the volume of hydrogen generated in the meantime, the number of moles of catalyst used and the relative catalytic loss calculated from the CV analysis done after CPE (Fig. S12(a)). Thus, a TON of 1172 was observed after the calculation.[24] The mass spectrum of complex **1** after CPE clearly exhibited the addition of a proton to the complex skeleton (metal centre) (Fig. S11(b)). To investigate the effect of different acids on the catalytic activity of **1**, we also used acetic acid, orthophosphoric acid and hydrochloric acid along with the same electrochemical parameters (Fig. S14) used for perchloric acid. The trend of activity of **1** was as follows: perchloric acid > hydrochloric acid > orthophosphoric acid > acetic acid, with TOF values, for the reduction of proton, of 1679, 10.15, 9.02 and 0.768 s^{-1}, respectively.

Thus, with the electrochemical analysis and the mass spectroscopic data, we propose that the reduction of proton occurs through two consecutive one-electron reduction reactions, leading to $Cu^{II}Cu^{II}/Cu^{II}Cu^{I}$ and $Cu^{II}Cu^{II}/Cu^{I}Cu^{I}$. Later, a proton may be transferred from the medium to one of the metal centers, forming the Cu^{I}–H species. Then, a –H from the water molecules dangling from the copper metal center makes a H···H bond, which generates a dihydrogen in the last step[25] (Fig. S11(b) and S25(a)).

$$\frac{i_{cat}}{i_p} = n \Big/ 0.4463(RTk/Fv)^{1/2} \quad \text{(A)}$$

OER study

The CV exhibited a pH-dependent irreversible peak at 0.96 V *vs.* Ag/AgCl (aqueous) (1.07 V *vs.* Ag/AgCl (aqueous) in DPV), attributed to the $Cu^{II}Cu^{II}/Cu^{II}Cu^{III}$ redox couple (Fig. 4). The same peak was found to be the catalytic peak for water oxidation when subjected to electrochemical catalysis at different pH values ranging from 7 to 13.5. Another irreversible peak was observed for the $Cu^{II}Cu^{II}/Cu^{II}Cu^{I}$ couple of complex **1** at 0.24 V *vs.* Ag/AgCl (aqueous) (0.15 V *vs.* Ag/AgCl in DPV (aqueous)) at a scan rate of 100 mV s^{-1}. The complex reported herein showed no change in the irreversible nature of the $Cu^{II}Cu^{II}/Cu^{II}Cu^{I}$ couple upon changing the scan rate from 2 mV s^{-1} to 80 mV s^{-1} (Fig. 6(A)).[26] **1** exhibited the highest efficiency for OER at pH 13.5. The overpotential values of **1** for OER catalysis at different pH values are provided in Table 1. The electrocatalytic TOF or the K_{cat} of complex **1** was calculated by the peak current method using eqn (S1) and (S2). The diffusion coefficient was also calculated using the same equation. Thus, by employing eqn (B) along with the slope of the graph depicting i_{cat}/i_p *vs.* square root of the scan rate (Fig. 6(B)), the TOF of **1** was calculated to be 9 s^{-1}.

$$\frac{i_{cat}}{i_p} = 1.43 {k_{cat}}^{1/2} \nu^{-1/2} \quad \text{(B)}$$

Electrochemical OER catalysis by **1** was also examined by changing the concentration of complex **1** in the aqueous buffer solution at pH 13.5 (Fig. S15). It was observed that the catalysis of the complex in these experimental conditions was completely

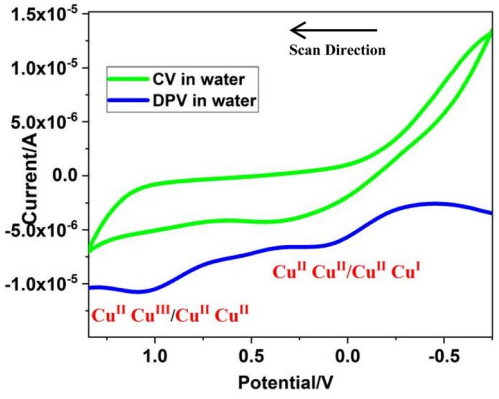

Fig. 4 CV and DPV of the anodic segment of **1** in water; $c = 0.25$ mM, scan rate = 100 mV s^{-1}, and internal reference: Fc/Fc^{+}.

Table 1 Overpotentials of complex **1** at different pH values during catalysis (calculated using $E = 1.23 - 0.059$ pH)

pH (buffer solution)	Experimental potential value for Cu^{II}/Cu^{III}	Overpotential
7	1.29 V	470 mV
8	1.30 V	540 mV
9	1.31 V	610 mV
10	1.30 V	660 mV
11	1.31 V	730 mV
12	1.32 V	790 mV
13	1.33 V	868 mV
13.5	1.33 V	900 mV

independent of the concentration of the complex in the solution, delineating a WNA pathway. The pH-based electrochemical data (Fig. 5(A)) of complex **1** are available in Table 1, and using the same information, a Pourbaix diagram is constructed (Fig. 5(B)). CPE was performed at +1.45 V *vs.* Ag/AgCl (aqueous) with 0.5 mM complex **1**. The results of CPE revealed a faradaic efficiency of ~84% and a TON of 66 under the given experimental conditions (Fig. S12(b)). Gas chromatography results obtained after 2 hours of CPE at +1.45 V *vs.* Ag/AgCl are added in Fig. S8. The mass spectrum of the solution after 2 hours of CPE displayed a peak at $m/z = 688.15$, which might be attributed to the $[Cu_2L_2–O–O–H]^+$ species, an expected intermediate in the WNA (water nucleophilic attack) pathway, along with a peak of the precursor of the WNA step at $m/z = 672.16$ (Fig. S11(a)). The calculation of TOF using FOWA (foot of the wave analysis) was done based on the CV results obtained at pH 13.5 (conc. = 0.5 mM, scan rate = 100 mV s^{-1}). The i_c/i_p *vs.* $1/\{1 + e[(E^{0,ap} - E)(F/RT)]\}$ plot was drawn to calculate the slope starting from the foot of the wave zone and, hence, to calculate the K_{WNA} of **1** in the WNA pathway. The value of TOF obtained from the FOWA was 31 s^{-1} (K_{WNA}) (Fig. 7). To prove that complex **1** is a suitable catalyst, 100 consecutive CV cycles were performed at pH 13.5 using the standard experimental conditions. During CV, it was observed that the current intensity

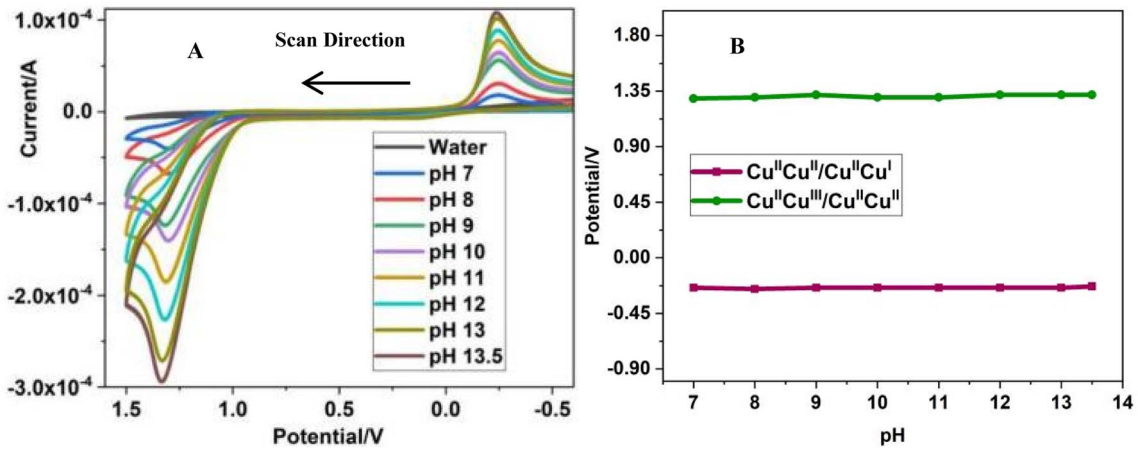

Fig. 5 (A) CV curves of complex **1** in phosphate buffer from pH 7–13.5 at a scan rate of 100 mV s^{-1} and 0.5 mM concentration using glassy carbon as the working electrode. (B) Pourbaix diagram of complex **1**.

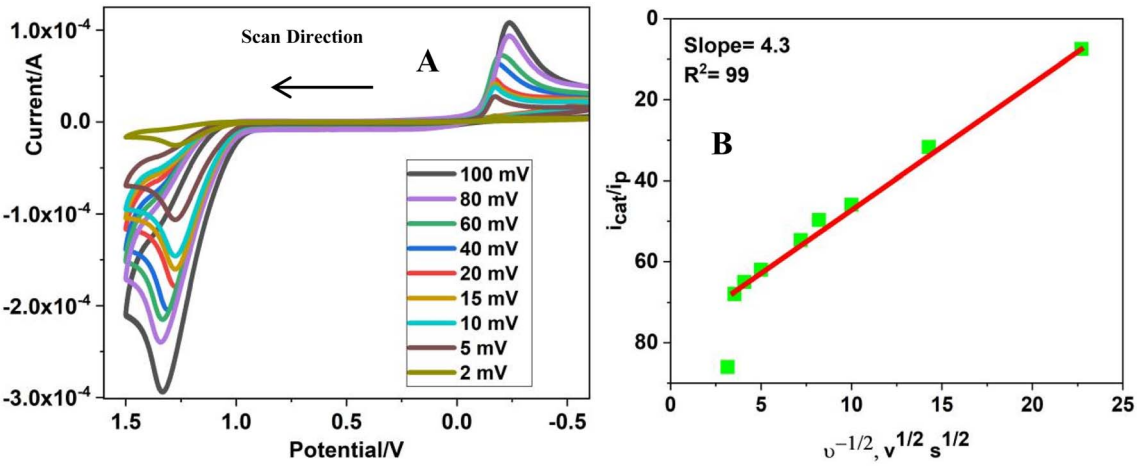

Fig. 6 (A) CV of 0.5 mM complex **1** in phosphate buffer at pH 13.5 with increasing scan rates from 2 mV s^{-1} to 100 mV s^{-1}. (B) The plot of i_{cat}/i_p as a function of the inverse of the square root of the scan rates used in the experiment of complex **1**.

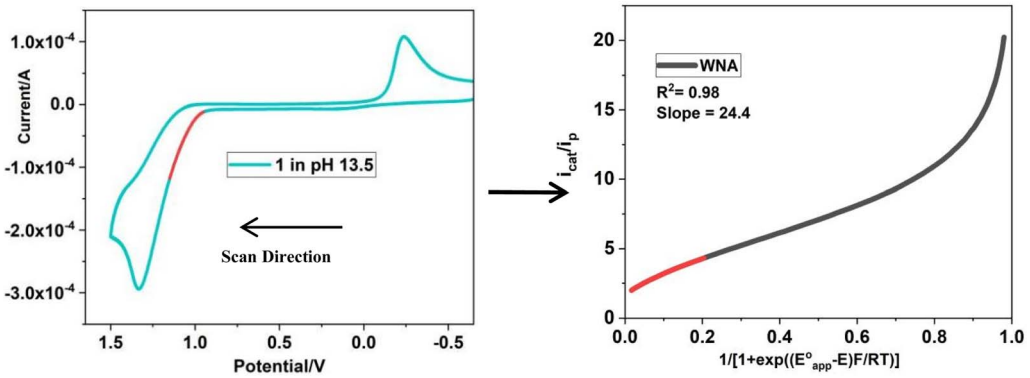

Fig. 7 The cyan line shows the CV curve of complex **1** (0.5 mM) at pH 13.5. The red line indicates the data points used for the FOWA. The i/i_p *vs.* $1/\{1 + e[(E^{0,ap} - E)(F/RT)]\}$ plot assuming a WNA. The fitting points for the extraction of rate constants at the foot of the wave are taken from the WNA graph. The red line indicates the points taken into consideration for the calculation of TOF.

decreased after the completion of each cycle. After the completion of 100 cycles, the working electrode was rinsed with distilled water, and a CV test was done in a fresh pH 13.5 buffer solution without the catalyst. This CV curve exhibited no sign of catalytic activity, showing that there was no accumulation of any metal oxide particles or precatalyst. The decrease in current during consecutive cycling may be due to the accumulation of oxygen gas on the working electrode. FESEM and EDX analyses of the working electrode were also done before and after the 100 CV cycles to investigate if any metal oxide traces were accumulated on the electrode. In agreement with our postulation, no trace of CuO_x nanoparticles was observed in the EDX analysis; rather, only elements of the buffer solution were observed at higher concentrations. Catalysis at such high pH raises the concern of molecular disintegration into nanoparticles in solution. Thus, DLS analysis of the complex solution was also carried out after CPE for 2 hours at +1.45 V. Since a majority of the particles observed in the DLS were found to be around ~1 micron, this negates the possibility of the generation of CuO_x nanoparticles in the catalytic solution (Fig. S9). To analyze the homogeneity of complex **1**, CV was repeated after CPE. An irreversible peak was observed for the $Cu^{II}Cu^{II}/Cu^{II}Cu^{I}$ couple from −0.24 V *vs.* Ag/AgCl before CPE at pH 13.5; later, a catalytic loss of 17.56% was observed in the CV curve recorded. The catalytic curve of the $Cu^{II}Cu^{II}/Cu^{II}Cu^{III}$ couple was observed with a loss in current density by a few percent, but the other curve of the $Cu^{II}Cu^{II}/Cu^{II}Cu^{I}$ couple remained exactly the same. This certifies that the catalyst remained in a homogeneous state in the buffer solution throughout catalysis, even at such a highly oxidative condition[27] (Fig. S13). As the mass spectral data and electrochemical analysis (Fig. S15) affirmatively indicate the WNA pathway and identify the intermediates formed during the oxidation of water to molecular oxygen[28–31] by **1**, the parent catalyst molecule may undergo one-electron oxidation to generate the Cu^{II}/Cu^{III} species, followed by the formation of a hydroxo intermediate (Fig. S11(a)). Later, **1** may undergo a proton coupled electron transfer (PCET) process, which possibly forms the peroxo radical. Finally, the attack on copper by one water molecules releases molecular oxygen, along with the regeneration of the catalyst. We have presented a plausible mechanism in Fig. S25(b).

CO_2RR study

Homogeneous CO_2RR (carbon dioxide reduction reaction)[32] by complex **1** was studied using a 0.5 mM aqueous solution of the catalyst by means of cyclic voltammetry (within the potential range from 1.50 V to −2.22 V *vs.* Ag/AgCl) and controlled potential electrolysis of an aqueous CO_2 purged solution of **1**. An initial run of CV with the catalyst solution was followed by CO_2 purging of the bulk solution for 60 minutes. The CV scan in the aforementioned potential range did not enhance the catalytic peak current to a significant extent. On adding the acid, the peak current increased at two places: −1.22 V and −1.85 V, corresponding to proton reduction and CO_2 reduction, respectively. The increment was noticed up to 8 equivalents of acid. A 14.3-fold increment in catalytic current was recorded for the CO_2RR activity (Fig. 8). The UV-visible spectra displayed a mild decrease in absorbance, with no change in the spectra after the addition of acid to the catalytic solution purged with carbon dioxide. Gas chromatography and HPLC were employed to analyze the reduction products in the gas phase and solution, respectively. CPE at −2.15 V *vs.* Ag/AgCl with 0.5 mM of **1** (purged with CO_2 for 60 minutes) for 270 minutes resulted in 24.1 coulomb charge. During CPE,[33] the reaction mixture was screened by mass spectroscopy for the identification of intermediates produced during catalysis[34,35] (Fig. S11(c)). For the analysis of the gaseous product, a constant volume of the gas mixture from the headspace of the coulometry cell was injected into the GC. GC traces showed the presence of three types of reduction products, namely H_2, CO and CH_4. However, the amount of the gases produced was very less. The TOF, TON and FE for CO and CH_4 were obtained as 0.045 h^{-1}, 0.20, and 0.08% and 0.05 h^{-1}, 0.22 and 0.36%, respectively. In order to identify the product in the solution, using a similar methodology, a fixed amount (20 μL) of the reaction mixture was injected into the HPLC at regular time intervals. The HPLC plot showed the presence of only oxalic acid. Therefore, in the CO_2RR, oxalic acid, methane and CO were obtained. For all the products, the

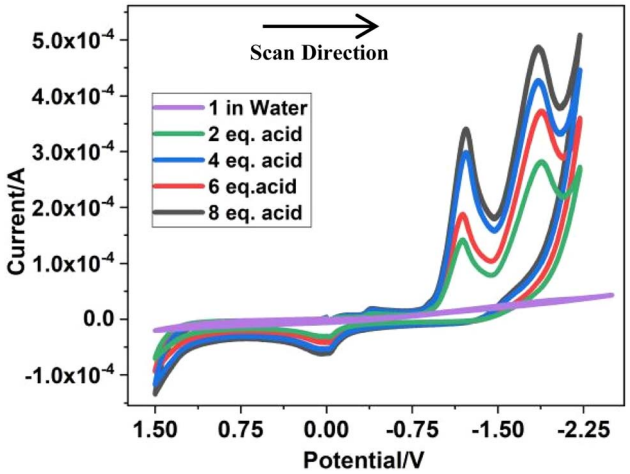

Fig. 8 CV curves of 0.5 mM complex **1** in water after 60 minutes of purging with CO_2 and consecutive addition of perchloric acid. Scan rate = 100 mV s^{-1}, internal reference: Ag/AgCl (aqueous), working electrode: glassy carbon.

number of moles produced was quantified. From this data, we calculated the % selectivity of 99.9% for oxalic acid.

In the line with the literature on CO_2RR by polynuclear copper complexes,[35,36] we identified **1**-*CHO (a peak at m/z = 702.23), **1**-H (m/z = 647.17), **1**-$C_2O_4H_2$ (m/z = 763.47) in the LCMS analysis (Fig. S11(c)). However, on HRMS, oxalate ions (Fig. S24) were observed, delineating the formation of oxalic acid during the electrocatalytic reduction of carbon dioxide. The formation of hydrogen has already been discussed in the HER study. Here, the most important feature is the very high selectivity to oxalic acid, with a faradaic efficiency of 92%, a TOF of 4 h^{-1} and a TON of 18 (HPLC plots in Fig. S22 and S23). The almost exclusive formation of oxalic acid may be due to the binuclear copper center, which provides the required stereochemical disposition to catch two $CO_2^{\bullet}$ radicals (one with each metal) in the void space between the two parallel pyridine rings, stabilizing them through π–π interactions between the pyridine ring and the CO_2 π electrons. This arrangement readily leads to C–C bond formation between the radicals to form an oxalato bridge.[37] In an electrochemical process, two consecutive one electron reduction reactions occur to form Cu^I–Cu^I. Each Cu^I is coordinated by CO_2. Coordinated CO_2 is then converted to $CO_2^{\bullet}$ radicals. The close approach of the $CO_2^{\bullet}$ radicals then forms the C–C bond to produce oxalate. Then, two protons are added to release oxalic acid and regenerate **1**. Thus, the plausible mechanism delineating CO_2RR is given in SI (Fig. S25(c)).

Theoretical calculations using DFT

DFT[38] calculations using the B3LYP[39,40] functional and DGTZVP basis set[41] were employed to analyze and optimize complex **1** in the IEFPCM[42] continuum solvation model with water as the solvent. The optimized structure (Fig. 9) yielded the minimum

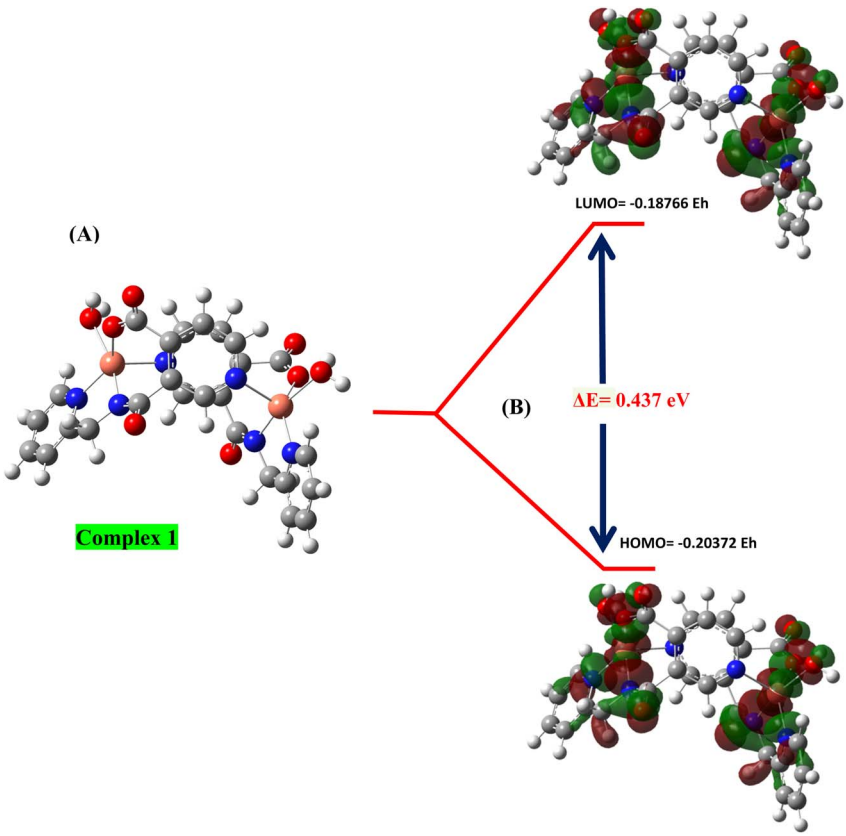

Fig. 9 (A) Optimized structure of complex **1**. (B) Theoretically calculated HOMO–LUMO gap of complex **1**.

energy geometry of catalyst **1**, along with the electronic energy and thermochemical data. Atomic ESP and Mulliken charge[43,44] distribution were calculated (Fig. S17). The ESP[7,45] plot (Fig. S26) exhibited that the electron density is highly localized around the carbonyl, acidic and aquo oxygen atoms. Since equal and identical kinds of oxo bonds are borne by both the metal centers, high electron density is observed around both the copper centers. The theoretical HOMO–LUMO gap[41] was calculated using the data observed, which provided a particularly low energy difference of $\Delta E = 0.437$ eV.[35] This value can be attributed to high electron transport and reactivity in the catalytic solution. This can be the reason behind the high activity of the complex.

Materials

Pyridine-3,4-dicarboxylic acid, thionyl chloride, 2-(aminomethyl)pyridine, triethylamine, copper carbonate (for the preparation of copper perchlorate), perchloric acid, disodium hydrogen phosphate, trisodium phosphate, sodium hydroxide and all the AR-grade solvents were procured from Spectrochem and used without further purification. The HPLC-grade solvents and oxalic acid, which was used as the reference in HPLC, were procured from Sigma-Aldrich. 99.99% pure CO_2 procured from Sam Air Products & Equipment, India, was used in the electrochemical reduction assays.

Characterization

All electrochemical analyses were performed using a CHI-6003E potentiostat with a 3-electrode setup (glassy carbon (GC), platinum wire and Ag/AgCl) at a 100 mV s^{-1} scan rate unless mentioned otherwise. UV-visible spectra were recorded on a PerkinElmer (Lambda 750) spectrophotometer. For LC-MS studies, a Thermo Scientific (USA) UltiMate 3000 was used. To analyze the gas, a trace 1110 gas chromatograph from Thermo Fisher Scientific was used. The FESEM analysis was performed on a Sigma 300 from Carl Zeiss Microscope Ltd, Germany, equipped with JSM 6390 LV from Jeol, Japan, for EDS. HPLC was performed using a Waters 2487 Dual λ Absorbance Detector. For DFT analysis, Gaussian 16 (ref. 46) was used, and GaussView 6.0.16 (ref. 47) was employed for visualizing the optimized structures.

Conclusions

This electrochemical study reveals the trifunctional nature of the water-soluble electrocatalyst **1**, with high reducing ability and a moderately efficient oxidizing ability in generating H_2, O_2 and $(COOH)_2$ in the aqueous medium. The identification of $[Cu_2L_2–O–O–H]^+$ on the mass spectra, along with the independence of K_{WNA} on the concentration of the catalyst, proves that **1** follows a WNA pathway for OER. The water molecule coordinated to the Cu metal center plays a crucial role in the generation of H_2, because the hydrogen atom in the Cu^I–H bonds and the hydrogen atom of water molecules form H···H bonds. This probable intramolecular H···H bond formation can be the reason for such a high HER efficiency of **1**. For CO_2RR, the dinuclear nature of the complex facilitates the generation of a C–C bond between two $CO_2^{\bullet-}$ radicals, hence generating an oxalato bridge efficiently. Analysis of products in the gas phase using gas chromatography quantified H_2, O_2, CO and CH_4, whereas HPLC was employed to detect and quantify the amount of oxalic acid produced after CPE in the catalytic solution with CO_2 and acid. Theoretical calculations engendered a very low HOMO–LUMO gap of 0.437 eV, which facilitates such a high activity of the homogeneous catalyst. The crucial intermediates formed during the reduction of protons to dihydrogen and carbon dioxide to oxalic acid as the major products, along with oxidation of water to molecular oxygen, were identified from the LC-MS spectra recorded after CPE at respective potentials. The HRMS spectra identified the formation of oxalate ions after CPE at −2.15 V for carbon dioxide reduction. Thorough exploration of the mechanisms *via* computational analysis using DFT is underway.

Author contributions

Md. Adnan Khan – methodology, formal analysis, data curation. Sonal Shruti – methodology. Swaraj Sengupta – formal analysis. Sahanwaj Khan – methodology. Prabhakar Bhardwaj – formal analysis. Pankaj Kumar – data curation. Subhendu Naskar – conceptualization, funding acquisition, supervision, writing, review and editing.

Conflicts of interest

There are no conflicts to declare.

Data availability

CCDC 2388873 (metal complex $Cu_2L_2 \cdot 2H_2O$) and CCDC 2388874 (ligand) contain the supplementary crystallographic data for this paper.[48a,b]

The data supporting this article have been included as part of the supplementary information (SI). Supplementary information is available. See DOI: **https://doi.org/10.1039/d5ra07824e**.

Acknowledgements

S. N. thanks SERB, New Delhi, Government of India, for funding this work through the SERB Project ("CRG/2023/001349" dated 15 March, 2024). S. N. acknowledges the NMR spectroscopic facility and computational facility in the Department of Chemistry, BIT Mesra, supported by the DST FIST Program (SR/FST/CSI-242/2012). The single-crystal X-ray diffraction facility and other analytical services availed from CIF, BIT Mesra, are greatly acknowledged. The authors also acknowledge the Department of Chemical Engineering, BIT Mesra, for gas chromatography and high-performance liquid chromatography measurements.

References

1 F. Li and J. B. Baek, *Nat. Catal.*, 2019, **2**, 477–478.
2 L. M. Salonen, D. Y. Petrovykh and Y. V. Kolen'ko, *Mater. Today Sustain.*, 2021, **11**, 100060.
3 Z. N. Zahran, Y. Tsubonouchi, E. A. Mohamed and M. Yagi, *ChemSusChem*, 2021, **9**, 1775–1793.
4 M. Sutradhar, A. J. L. Pombeiro and J. A. L. da Silva, *Coord. Chem. Rev.*, 2021, **439**, 213911.
5 A. M. R. Ramírez, S. Heidari, A. Vergara, M. Villicaña Aguilera, P. Preuss, M. B. Camarada and A. Fischer, *ACS Mater. Au*, 2023, **3**, 177–200.
6 M. A. Khan, S. Khan, S. Sengupta, B. N. Mongal and S. Naskar, *Coord. Chem. Rev.*, 2024, **504**, 215679.
7 M. Raj, K. Makhal, A. Mishra, B. S. Mallik and S. K. Padhi, *Inorg. Chem.*, 2023, **62**, 10993–11008.
8 M. D. Kärkä, O. Verho, E. V. Johnston and B. Åkermark, *Chem. Rev.*, 2014, **114**, 11863–12001.
9 Y. Han, Y. Wu, W. Lai and R. Cao, *Inorg. Chem.*, 2015, **54**, 5604–5613.
10 J.-W. Wang, X.-Q. Zhang, H.-H. Huang and T.-B. Lu, *ChemCatChem*, 2016, **8**, 3287–3293.
11 T. Nakazono, A. R. Parent and K. Sakai, *Chem. Commun.*, 2013, **49**, 6325–6327.
12 X. Zhong, H.-J. Peng, C. Xia and X. Liu, *J. Mater. Chem. A*, 2024, **12**, 19663–19684.
13 S. L. Jain, P. Bhattacharyya, H. L. Milton, M. Z. Slawin, J. A. Crayston and J. Derek Woollins, *Dalton Trans.*, 2004, **6**, 862–871.
14 R. C. DiDomenico, K. Levine, L. Reimanis, H. D. Abruña and T. Hanrath, *ACS Catal.*, 2023, **13**, 4938–4948.
15 T.-T. Li and Y.-Q. Zheng, *Dalton Trans.*, 2016, **45**, 12685–12690.
16 G. Ruan, P. Ghosh, N. Fridman and G. Maayan, *J. Am. Chem. Soc.*, 2021, **143**(28), 10614–10623.
17 E. Ahmad, K. Majee, J. Patel, B. Das and S. K. Padhi, *Eur. J. Inorg. Chem.*, 2017, **28**, 3409–3418.
18 P. Garrido-Barros, D. Moonshiram, M. Gil-Sepulcre, P. Pelosin, C. G. Suriñach, J. B. Buchholz and A. Llobet, *J. Am. Chem. Soc.*, 2020, **142**, 17434–17446.
19 O. V. Dplomanov, L. J. Bourhis, R. J. Gildea, J. A. K. Howard and H. Puschmann, *Acta Crystallogr., Sect. A:Found. Adv.*, 2015, **71**, 59–75.
20 T. Fang, L.-Z. Fu, L.-L. Zhou and S.-Z. Zhan, *Electrochim. Acta*, 2015, **161**, 388–394.
21 H. A. Younus, H. Emam, N. Ahmad, M. Negm, M. Alomar, F. M. Elantabli, M. M. El-Rabiei, R. A. Hajri, S. Zhang and M. A. Abri, *ChemElectroChem*, 2024, **11**, e202300710, DOI: 10.1002/celc.202300710.
22 S. Nestke, M. Kügler, J. Scholz, M. Wilken, C. Jooss and I. Siewert, *Eur. J. Inorg. Chem.*, 2017, **28**, 3376–3382.
23 A. Z. Haddad, S. P. Cronin, M. S. Mashuta, R. M. Buchanan and C. A. Grapperhaus, *Inorg. Chem.*, 2017, **56**, 11254–11265.
24 S. Karim, A. Chakraborty, D. Samanta, E. Zangrando, T. Ghosh and D. Das, *Catal. Sci. Technol.*, 2020, **10**, 2830–2837.
25 M. Raj, K. Makhal, D. Raj, A. Mishra, B. S. Mallik and S. K. Padhi, *Dalton Trans.*, 2023, **52**, 17797–17809.
26 T. Zhang, C. Wang, S. Liu, J.-L. Wang and W. Lin, *J. Am. Chem. Soc.*, 2014, **136**(1), 273–281.
27 G. Ruan, L. Engelberg, P. Ghosh and G. A. Maayan, *Chem. Commun.*, 2021, **57**, 939–942.
28 S. Khan, S. Sengupta, M. A. Khan, M. P. Sk, N. Ch. Jana and S. Naskar, *Inorg. Chem.*, 2024, **63**, 1888–1897.
29 S. Khan, S. Sengupta, M. A. Khan, M. P. Sk and S. Naskar, *Dalton Trans.*, 2023, **52**, 7590.
30 M. A. Khan, S. Khan, S. Sengupta and S. Naskar, *New J. Chem.*, 2025, **49**, 6963–6974.
31 X. Zhang, Y.-Y. Li, J. Jiang, R. Zhang, R.-Z. Liao and M. Wang, *Inorg. Chem.*, 2020, **59**, 5424–5432.
32 V. Boor, J. E. B. M. Frijns, E. PerezGallent, E. Giling, A. T. Laitinen, E. L. V. Goetheer, L. J. P. vandenBroeke, R. Kortlever, W. de Jong, O. A. Moultos, T. J. H. Vlugt and M. Ramdin, *Ind. Eng. Chem. Res.*, 2022, **61**, 14837–14846.
33 L.-L. Zhou, T. Fang, J.-P. Cao, Z.-H. Zhu, X.-T. Su and S.-Z. Zhan, *J. Power Sources*, 2015, **273**, 298e304.
34 S. K. S. Akhter, D. Srivastava, A. Mishra, N. Patra, P. Kumar and S. K. Padhi, *Chem.–Eur. J.*, 2024, **30**, e202403321.
35 J.-W. Liu, D. Peng, S.-J. Liu, H.-R. Wen, Z. H. Zhu, J. Zhao and J. L. Chen, *ACS Sustainable Chem. Eng.*, 2025, **13**, 2564–2573.
36 Z. Zhang, Y. Yang, J. Wang, Xu. Jing and C. Duan, *Inorg. Chem. Front.*, 2025, **12**, 5389–5396.
37 S. Sengupta, S. Khan, B. N. Mongal, W. Lewis, M. Fleck, S. K. Chattopadhyay and S. Naskar, *Polyhedron*, 2020, **191**, 114798.
38 K. Ye, Y. Li and R. Liao, *RSC Adv.*, 2016, **6**, 90035–90045.
39 M. M. Ibrahim, G. A. M. Mersal, A. M. Fallatah, K. Althubeiti, H. S. El-Sheshtawy, M. F. A. Taleb, M. R. Das, R. Boukherroub, M. S. Attia and M. A. Amin, *RSC Adv.*, 2022, **12**, 8030.
40 J. M. Dressel, E. N. Cook, S. L. Hooe, J. J. Moreno, D. A. Dickie and C. W. Machan, *Inorg. Chem. Front.*, 2023, **10**, 972–978.
41 M. Khajehzadeh, M. Moghadam, S. Rahmaniasl and M. Rajabi, *J. Mol. Struct.*, 2021, **1230**, 129660.
42 A. Ramdass, V. Sathish, M. Velayudham, P. Thanasekaran, S. Umapathy and S. Rajagopal, *RSC Adv.*, 2015, **5**, 38479.
43 F. Ma and X. Chen, *ACS Appl. Nano Mater.*, 2023, **6**, 16546–16554.
44 Z. Jiang, W. Sun, H. Shang, W. Chen, T. Sun, H. Li, J. Dong, J. Zhou, Z. Li, Y. Wang, R. Cao, R. Sarangi, Z. Yang, D. Wang, J. Zhang and Y. Li, *Energy Environ. Sci.*, 2019, **12**, 3508.
45 E. Paul, R. Raza, S. R. Dhara, N. Baildya and K. Ghosh, *RSC Adv.*, 2024, **14**, 32759–32770.
46 M. J. Frisch, G. W. Trucks, H. B. Schlegel, G. E. Scuseria, M. A. Robb, J. R. Cheeseman, G. Scalmani, V. Barone, G. A. Petersson, H. Nakatsuji, X. Li, M. Caricato, A. V. Marenich, J. Bloino, B. G. Janesko, R. Gomperts, B. Mennucci, H. P. Hratchian, J. V. Ortiz, A. F. Izmaylov, J. L. Sonnenberg, D. Williams-Young, F. Ding, F. Lipparini, F. Egidi, J. Goings, B. Peng, A. Petrone, T. Henderson, D. Ranasinghe, V. G. Zakrzewski, J. Gao, N. Rega, G. Zheng, W. Liang, M. Hada, M. Ehara, K. Toyota, R. Fukuda, J. Hasegawa, M. Ishida, T. Nakajima, Y. Honda,

O. Kitao, H. Nakai, T. Vreven, K. Throssell, J. A. Montgomery Jr, J. E. Peralta, F. Ogliaro, M. J. Bearpark, J. J. Heyd, E. N. Brothers, K. N. Kudin, V. N. Staroverov, T. A. Keith, R. Kobayashi, J. Normand, K. Raghavachari, A. P. Rendell, J. C. Burant, S. S. Iyengar, J. Tomasi, M. Cossi, J. M. Millam, M. Klene, C. Adamo, R. Cammi, J. W. Ochterski, R. L. Martin, K. Morokuma, O. Farkas, J. B. Foresman and D. J. Fox, *Gaussian 16, Revision A.03*, Gaussian, Inc., Wallingford CT, 2016.

47 R. Dennington, T. A. Keith and J. M. Millam, *GaussView 6.0. 16*, Semichem Inc., Shawnee Mission, 2016.

48 (*a*) CCDC 2388873: Experimental Crystal Structure Determination, 2025, DOI: **10.5517/ccdc.csd.cc2l5tf1**; (*b*) CCDC 2388874: Experimental Crystal Structure Determination, 2025, DOI: **10.5517/ccdc.csd.cc2l5tg2**.